Primary processes in photosynthesis: what do we learn from high-field EPR spectroscopy?

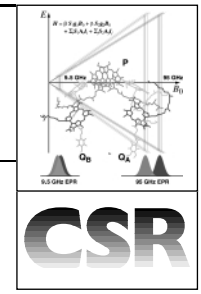

Klaus Möbius

Department of Physics, Free University Berlin, Arnimallee 14, D-14195 Berlin, Germany

Received 9th August 1999

Primary photosynthesis is the biological electron transfer process by which green plants and certain bacteria convert the energy of sunlight into electrochemical energy. Light-induced charge separation is achieved by (bacterio) chlorophyll donor and quinone acceptor cofactors in the transmembrane reaction center protein complexes. Thereby transient radical ions are formed creating weakly coupled radical pairs. Time-resolved high-field EPR spectroscopy is ideally suited to study such short-lived species in their working states. It provides detailed information on the structure and dynamics of the cofactors in their binding sites and on hydrogen bond interaction with the protein. Thereby, our understanding of primary photosynthesis on the molecular level is improved.

1 Introduction

As we all know, it is photosynthesis that enables life on Earth by converting the energy of sunlight into electrochemical energy that is needed by higher organisms for synthesis, growth and replication. Photosynthetic processes span a gigantic range of time-scales of, at least, 20 orders of magnitude, ranging from less than 100 fs to more than 100 Ms. Consequently, photosynthesis is dealt with in vastly different fields of research, such as radiation and condensed phase physics, photo- and biochemistry, physiology and botany. The so-called primary processes of photosynthesis are those in which the incoming light quanta, after being harvested from 'antenna' pigment–protein complexes and channeled to the 'reaction center' (RC) complexes by ultra-fast energy transfer, initiate electron transfer (ET) reactions between protein-bound donor and acceptor pigments across the cytoplasmic membrane. The successive charge-separating ET steps that occur between the various redox partners in the transmembrane RC have very different reaction rates, k_{ET}, the lifetimes, $t_{1/2} = (k_{ET})^{-1}$, of the transient charge-separated states ranging from less than 1 ps for neighboring donor–acceptor pigments to more than 1 ms for large donor–acceptor separations on opposite sides of the membrane (*ca*. 40 Å). The cascade of charge-separating ET steps of primary photosynthesis competes extremely favorably with wasteful charge-recombination ET steps providing unitary quantum yield. This unique feature of the RC has stimulated world-wide research activities to understand the structure–function relationship of primary photosynthesis on the molecular level. In the last decade, remarkable progress has been made in this understanding, mostly from biochemical and biophysical investigations including X-ray crystallography, site-directed mutagenesis, ultra-fast laser spectroscopy in the visible and IR regions and, last but not least, modern EPR (electron paramagnetic resonance) techniques.[1,2]

Among these multiple technologies useful for investigating biological systems, EPR has a prominent role because many valence states of metals in metalloproteins are paramagnetic, and single-electron transfer reactions are quite common with paramagnetic intermediates. For characterizing the intermediates of the photosynthetic ET chain EPR, therefore, is one of the methods of choice, because transient radical ions and radical pair states are formed during the primary process. Hence, to set the stage for this overview on what we learn from high-field EPR spectroscopy in photosynthesis research, some more remarks seem to be appropriate concerning photosynthetic RCs, EPR spectroscopy in general, and high-field EPR in particular. To at least partially compensate for the compression of the material in this short overview, the reader is referred to several overviews that treat the subject in more detail.[1–5]

2 Photosynthetic reaction centers

The largest impact of photosynthesis on life on Earth is due to green plants and certain algae in whose RCs a reversible catalytic ET process occurs for which water serves as electron donor, carbon dioxide is fixed in the form of carbohydrates, and oxygen gas is released as a by-product [eqn. (1)].

$$H_2O + CO_2 \xrightarrow[\text{chlorophyll}]{h\nu} C(H_2O) + O_2 \qquad (1)$$

Klaus Möbius was born in 1936 in Berlin. After studying physics, mathematics and chemistry at the Free University Berlin (FUB), he did his PhD (Dr. rer.nat.) with R. Honerjäger on EPR spectroscopy of organic radicals. He worked as post-doc with A. H. Maki at the University of California, Riverside, in 1970. Since 1971 he has been working as Professor in the Department of Physics of the FUB, but also spent some time as Visiting Professor at the Indian Institute of Technology, Madras, in 1983, at the University of Padova in 1997 and, repeatedly since 1980, at the Hebrew University of Jerusalem. His scientific work was recognized by several international awards. Now his major research interest is concerned with the development of high-field/high-frequency EPR instrumentation, electron transfer in natural and artificial photosynthetic systems and in DNA-photolyase, and the structure and dynamics of site-directed spin labeled proteins.

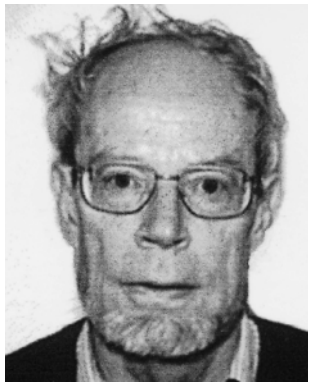

DOI: 10.1039/a706426h

For this photo-reaction to proceed, chlorophylls and other cofactors are needed as biocatalysts. Organisms capable of oxygenic photosynthesis use two light reactions associated with the Photosystem I (PS I) and Photosystem II (PS II) reaction centers in a sequential electron transport scheme, known as the

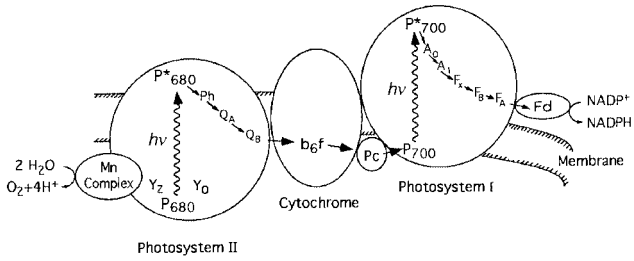

Fig. 1 Z-scheme of electron transfer in green plant photosystems I and II interconnected by the cytochrome b_6f and plastocyanin (Pc) complexes. Abbreviations: P_{680} and P_{700}, primary donors; Y_Z and Y_D, tyrosines; Mn complex, oxygen-evolving complex; Ph, pheophytin; Q_A and Q_B, quinones; A_0, chlorophyll; A_1, quinone; F_X, F_B, F_A, iron–sulfur centers; Fd, ferredoxin–flavoprotein complexes. Adapted from ref. 4.

Z-scheme[1] (Fig. 1), in which PS I and PS II operate in tandem. After light excitation of the primary donors, the chlorophyll dimers P_{700} and P_{680} which absorb predominantly at 700 and 680 nm, respectively, ET is achieved from the water-splitting Mn complex (*left*) *via* the cytochrome b_6f complex and PS I to $NaDP^+$ (*right*), where the coupling to the dark reactions for CO_2 fixation occurs. The ellipses in Fig. 1 represent the various protein–cofactor complexes. The vertical position of each cofactor indicates its redox potential. Light excitation of the primary donors to their first excited singlet states, P^*, is symbolized by wavy arrows *hν*. The other arrows signify the ET pathways.

The starting point for a detailed analysis of the primary ET processes on the molecular level is the three-dimensional structure of the RC protein complexes which recently became available. For oxygenic photosynthetic organisms, unfortunately, these structures could not yet be resolved to atomic resolution: for PS I of the cyanobacterium *Synechococcus elongatus*[6] to 4 Å, for PS II of green plants[7] to 8 Å. This is in contrast to the RCs of anoxygenic photosynthetic bacteria, such as the purple bacteria, for which X-ray crystallographic models are now refined to 2.3 Å resolution.[8]

Three billion years before green plants evolved, the Earth and its atmosphere were very different from what they are today. Nevertheless, photosynthetic energy conversion could be achieved by certain bacteria, for instance the purple bacteria *Rhodobacter (Rb.) sphaeroides* and *Rhodopseudomonas (Rps.) viridis*. These early photosynthetic organisms are simple, one-cellular protein-bound donor–acceptor complexes that contain only one RC for light-induced charge separation. They cannot split water, but rather use hydrogen sulfide or organic compounds as electron donors to reduce CO_2 to carbohydrates with the help of sunlight and bacteriochlorophyll as biocatalyst. The net reaction for this anoxygenic bacterial photosynthesis is given by eqn. (2).

$$2H_2S + CO_2 \xrightarrow[\text{bacteriochlorophyll}]{h\nu} C(H_2O) + H_2O + 2S \quad (2)$$

In Fig. 2 the structural arrangement of the RC of *Rb. sphaeroides* is sketched with the cofactor embedded in the L, M, H protein subunits.[8] Again, the vertical positions of the cofactors indicate their redox potentials. They span a range of approx. 1.5 V between the primary donor P_{865} (a bacteriochlorophyll a dimer) ground state and its first excited singlet state, P^*_{865}. It is intriguing that, despite the apparent two-fold local symmetry of the cofactor arrangement, the ET pathway is one-sided along the L subunit, as indicated by the arrows in Fig. 2. The origin of this 'unidirectionality' of bacterial ET, which is

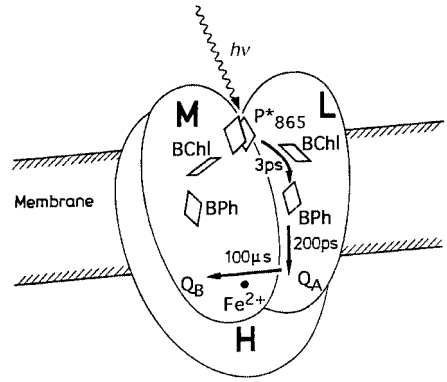

Fig. 2 Schematic arrangement of the cofactors in the reaction center of the photosynthetic bacterium *Rb. sphaeroides* with the L, M, and H protein subunits. The primary electron transfer proceeds solely along the L subunit with rates given as half-lifetimes $(k_{ET})^{-1}$ of the redox pairs. Abbreviations: P_{865}, primary donor $(BChl)_2$ dimer; BChl, bacteriochlorophyll a; BPh, bacteriopheophytin a; Q_A and Q_B, ubiquinones. Adapted from ref. 4.

a dominant motif in the evolution of bacteria, is not yet fully understood. In the following, the discussion will be restricted largely to anoxygenic bacterial RCs.

To conclude this section, it should be pointed out that, in parallel to the experimental accomplishments mentioned above, theory has contributed much during the last years for a better understanding of the primary processes in photosynthesis. Just to give some recent examples: ET routes and kinetic data could be interpreted in depth on the basis of the Marcus–Jortner theory.[9] Next to covalent bonds and van der Waals contacts, hydrogen bonds between cofactors and amino acid residues turned out to be of utmost importance in ET-proteins, as has been elucidated by extended pathway analysis of H-bond networks.[10] In addition to *static* donor–acceptor and cofactor–protein interactions, the protein *dynamics* can have pronounced effects on biological ET, in particular when molecular motion occurs on a time-scale comparable to that of the respective ET step.[11]

3 EPR spectroscopy

If a paramagnetic sample, for example with spin $S = 1/2$, is placed into an EPR spectrometer, the electron spins will align themselves with respect to the total magnetic field that arises both from the external Zeeman field B_0 and local 'hyperfine' fields from nearby magnetic nuclei. These nuclei possess magnetic moments, *i.e.*, their nuclear spin is $I \neq 0$, for example $I = 1/2$ for protons. For this situation, the static spin Hamiltonian, $\mathcal{H}_0$, that describes the spin interaction energies, consists of three terms [eqn. (3)], *i.e.*, the field-dependent

$$\mathcal{H}_0 / h = \frac{\mu_B}{h}\mathbf{B}_0 \cdot \tilde{g} \cdot \hat{\mathbf{S}} - \sum_i \frac{g_{ni}\mu_K}{h}\mathbf{B}_0\hat{\mathbf{I}}_i + \sum_i \hat{\mathbf{S}}\cdot\tilde{A}_i\cdot\hat{\mathbf{I}}_i \quad (3)$$

electron and nuclear Zeeman interactions and the field-independent electron–nuclear hyperfine interactions. (*h*: Planck constant; μ_B, μ_K: Bohr and nuclear magnetons; g_n: nuclear *g*-factor; $\hat{\mathbf{S}}$, $\hat{\mathbf{I}}$: electron and nuclear spin vector operators; the summation is over all nuclei).

The interaction tensors $\tilde{g}$ and $\tilde{A}_i$ are probing the electronic structure of the molecule *globally* ($\tilde{g}$ tensor) and *locally* (hyperfine tensors), respectively. In isotropic fluid solution, only the scalar values, 1/3 Tr($\tilde{g}$) and 1/3 Tr($\tilde{A}$), are observed. In frozen solutions, powders or single crystals, on the other hand, individual tensor components also become observable under appropriate resolution conditions. Thereby the information content of the EPR spectra is considerably enhanced in terms of molecular orientations with respect to $\mathbf{B}_0$.

In the strong field approximation, the energy eigenvalues of eqn. (3) are classified by the magnetic spin quantum numbers, m_S and m_I, and are given, to first order, by eqn. (4), where the

$$E_{m_S m_I}/h = \frac{g'\mu_B}{h} B_0 \cdot m_S - \sum_i \frac{g_{ni}\mu_K}{h} B_0 \cdot m_{I_i} + \sum_i A'_i \cdot m_S \cdot m_{I_i} \quad (4)$$

quantities g' and A' contain the desired information about magnitude and orientation of the interaction tensors. For single crystal samples the complete tensor information can be extracted from the angular dependence of the resonance lines when the crystal is rotated in its three symmetry planes ('rotation patterns'). If the $\tilde{g}$ and $\tilde{A}_i$ tensors are collinear, *i.e.*, have the same principal axes system (α, β, γ), their rotation patterns will have the same angular dependence. Let us, for instance, mount the crystal in such a way that the rotation axis is the *x*-axis of the molecular axes system (*x*, *y*, *z*) and is perpendicular to the $\mathbf{B}_0$ direction. Then the rotation occurs in the *yz* plane defining an angle θ as the angle between the *z*-axis and the field direction. For this situation, g' takes the form of eqn. (5) (notice that $\tilde{g}_{ij}^2$ denotes the components of the squared $\tilde{g}$ tensor). An analogous expression holds for A_i' in the limit of small *g*-anisotropy, as is typical for bioorganic systems as long as they do not contain transition metal ions. For the other two symmetry planes, *zx* and *xy*, the corresponding tensor components are found by cyclic replacement $y \rightarrow z \rightarrow x \rightarrow y$. As an example, let us consider a doublet radical ($S = 1/2$) in isotropic fluid solution containing four symmetry-equivalent protons in a

$$g' = (\tilde{g}_{yy}^2 \cdot \sin^2\theta + \tilde{g}_{zz}^2 \cdot \cos^2\theta + \tilde{g}_{yz}^2 \cdot \sin 2\theta)^{1/2} \quad (5)$$

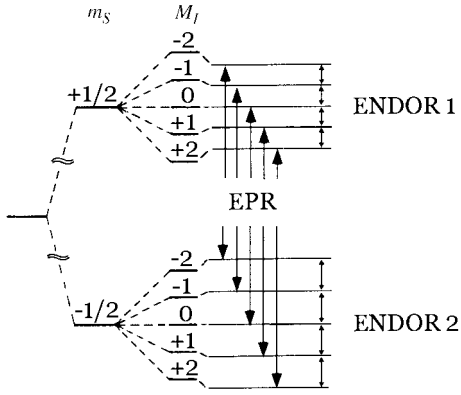

Fig. 3 High-field spin energy levels of a radical ($S = 1/2$) with a group of four equivalent protons ($I = 1/2$) dissolved in fluid solution. $M_I = \sum_i m_{I_i}$ is the total nuclear quantum number of the group.

strong B_0 field. Fig. 3 shows the energy level scheme according to eqn. (4), in which for isotropic solutions only scalar interaction parameters prevail. Following the selection rules $\Delta m_S = \pm 1$, $\Delta m_{I_i} = 0$, five EPR lines are observed with binominal intensity distribution owing to the first-order transition frequency degeneracies of equivalent nuclei. For large, low-symmetry radicals, such as those occurring in photosynthesis, with each set of inequivalent nuclei the number of EPR lines obviously increases in a multiplicative way. This results in strongly inhomogeneously broadened EPR spectra, and individual hyperfine lines can no longer be resolved.

For such cases, one can resort to electron-nuclear-double resonance (ENDOR) techniques.[12] In ENDOR the sample is irradiated simultaneously by two electromagnetic fields, a microwave field (to drive EPR transitions $\Delta m_S = \pm 1$) and a radio-frequency field (to drive NMR transitions $\Delta m_{I_i} = \pm 1$) (see Fig. 3). Under appropriate conditions, ENDOR signals are observed by monitoring the changes of EPR line amplitudes when sweeping the radio-frequency field through the nuclear resonance frequencies. Thus, every group of equivalent nuclei—no matter how many nuclei are involved and what their spin is—contributes only two ENDOR lines because, within an m_S manifold, the hyperfine levels are equidistant. The gain in resolution of ENDOR *versus* EPR, therefore, becomes very drastic for low-symmetry molecules because, with an increasing number of groups of nuclei, the number of ENDOR lines increases only in an additive way.

This gain in resolution becomes particularly pronounced when nuclei with different magnetic moments are involved. Their ENDOR lines appear in different frequency ranges, and from their Larmor frequencies these nuclei can be immediately identified. In the case of accidental coincidence of ENDOR lines from different nuclei at X-band EPR (9.5 GHz, 0.34 T) they can be separated when working at higher frequencies and Zeeman fields, for instance 95 GHz, 3.4 T, *i.e.*, when applying W-band ENDOR (see below).

For a doublet radical, the two ENDOR lines of a particular group of equivalent nuclei appear, to first order, at:

$$\nu^{\pm}_{\mathrm{ENDOR}} = |\nu_n \pm A/2| \quad (6)$$

with the free nuclear Larmor frequency $\nu_n = (g_n\mu_K/h)\cdot B_0$.

To illustrate the power of the ENDOR method, studies of the electron structure of the primary donor cation radical, $P_{865}^{+\cdot}$, of the RC of the photosynthetic purple bacterium *Rb. sphaeroides* are chosen as an example.[13] P_{865} is a bacteriochlorophyll dimer and, for a better understanding of the ET characteristics, the details of the electron distribution over the dimer halves are of prime interest. The best approach is, of course, to study single crystals of RCs in which $P_{865}^{+\cdot}$ is generated by light illumination. From the angular dependence of the hyperfine interactions in the three crystallographic planes, which could be resolved by ENDOR and electron-nuclear-nuclear-triple resonance, five complete proton hyperfine tensors could be determined. For the first time it was possible to distinguish ENDOR lines from protons on distinct halves, D_L and D_M, of the dimer. The result unambiguously shows that the unpaired valence electron is asymmetrically distributed over the dimer-halves, favoring D_L over D_M by 2:1.

Up to this point we have focused our discussion on paramagnetic systems with only one unpaired electron, $S = 1/2$. However, in photosynthesis and other areas of biochemistry, there are various paramagnetic centers of functional significance with $S > 1/2$. These are called 'high-spin' systems, prominent examples being the high-spin ions Fe^{2+} ($S = 2$), Fe^{3+} ($S = 5/2$) and high-spin Mn^{2+} ($S = 5/2$) in the distinct ligand fields of their protein complexes. Also photoexcited triplet states ($S = 1$) of chromophores are often studied to elucidate the electronic structure of relevant cofactors,[2] for example the primary donor P_{680} of PS II reaction centers of green plant photosynthesis.[14] For such systems it is necessary to add a 'fine-structure' term [eqn. (7)] to the Hamiltonian of eqn. (3), where $\tilde{D}$

$$\mathcal{H}_{SS}/h = \hat{\mathbf{S}}\cdot\tilde{D}\cdot\hat{\mathbf{S}} \quad (7)$$

is the spin–spin coupling or 'zero-field-splitting' tensor. For organic molecules $\tilde{D}$ is traceless. In the principal axes system of $\tilde{D}$ (here assumed to be collinear with the molecular axes system), eqn. (7) can be expressed as eqn. (8), where $-X$, $-Y$, $-Z$ are the zero-field energy values. This is normally rewritten in terms of the zero-field parameters D and E:

$$\mathcal{H}_{SS}/h = -X\hat{\mathbf{S}}_x^2 - Y\hat{\mathbf{S}}_y^2 - Z\hat{\mathbf{S}}_z^2 \quad (8)$$

$$\mathcal{H}_{SS}/h = D(\hat{\mathbf{S}}_z^2 - 1/3S(S+1)) + E(\hat{\mathbf{S}}_x^2 - \hat{\mathbf{S}}_y^2) \quad (9)$$

$$\text{with } D = 1/2\,(X+Y) - Z,\ E = -1/2(X-Y) \quad (10)$$

Fig. 4a sketches the energy levels of a triplet state molecule and the EPR transitions for a Hamiltonian that comprises only the Zeeman and fine structure terms. Fig. 4b includes the nuclear and hyperfine interaction terms resulting in additional

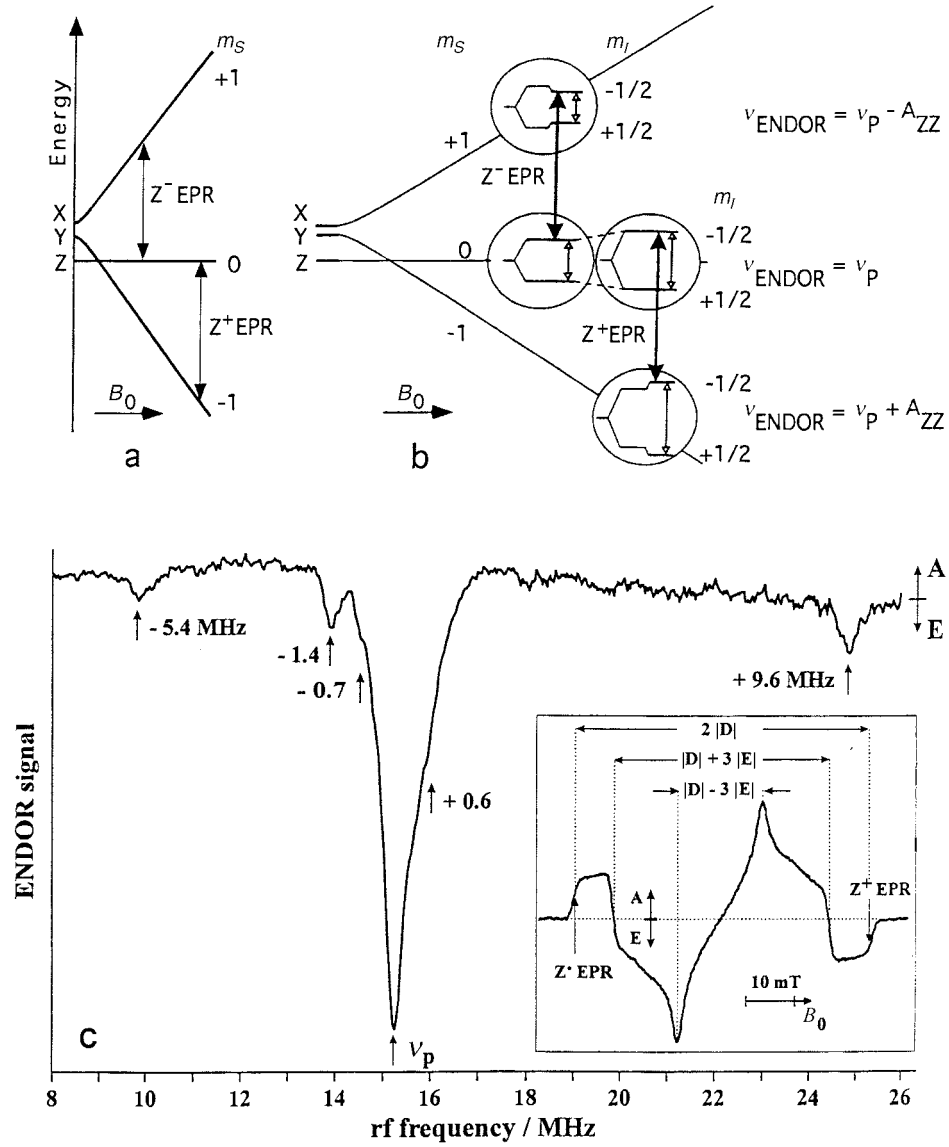

Fig. 4 (a) Spin energy levels of a triplet-state molecule ($S = 1$) when the triplet z-axis is parallel to the B_0 direction. Z^- and Z^+ are the allowed EPR transitions in the high-field limit. (b) First-order electron Zeeman, nuclear Zeeman and hyperfine splittings ($D > 0, A_{zz} > 0$). For each EPR transition, Z^- or Z^+, there are two ENDOR resonance frequencies at ν_p and $\nu_p - A_{zz}$ or at ν_p and $\nu_p + A_{zz}$, respectively. Here ν_p is the proton Larmor frequency and A_{zz} the hyperfine tensor component along the triplet z-axis. (c) Time-resolved spin-polarized EPR (inset) and ENDOR spectra of $^3P_{680}$ in frozen-solution PS II ($T = 15$ K). A, E stand for absorption, emission. The numbers on the ENDOR spectrum refer to A_{zz} components of the proton $\tilde{A}_i$ tensors.[14]

ENDOR transitions. Fig. 4c shows the ENDOR spectrum taken at the field position of the Z^+ EPR line.[14] Owing to the inherent resolution capability of ENDOR it was possible to conclude from the hyperfine couplings that at cryogenic temperatures the triplet state of photoexcited P_{680} in PS II is largely located on a monomeric chlorophyll a molecule of the dimeric P_{680}. This result confirms conclusions drawn earlier from optical and EPR work.

Although the fine-structure Hamiltonian is not field-dependent, there are, nevertheless, reasons to favour the study of high-spin systems by high-field EPR (see below), for instance, when the zero-field splitting D exceeds the microwave frequency ν_0 at X-band (9.5 GHz). For such a case, certain EPR transitions cannot be excited at all for any B_0 value, and larger microwave quanta are needed to record the whole spectrum. An example for such a biological high-spin system is metmyoglobin with $S = 5/2$ ferric heme, for which EPR transitions at 130 GHz became observable that were undetectable at X-band due to the large zero-field splitting.[15]

In the preceding paragraphs emphasis has been put on the discussion of *static* spin interaction energies; some of them are magnetic field-dependent (electron and nuclear Zeeman interactions), others are field-independent (fine-structure and hyperfine-structure interactions). EPR measurements at different field-frequency settings will, therefore, be a powerful tool to separate these different interactions from each other and optimize the spectral resolution. In the remaining paragraphs of this section we turn to modern time-resolved EPR methods which have been developed to study *time-dependent* parts of the Hamiltonian, *e.g.* molecular motion, spin dynamics and relaxation.

Fig. 5 summarizes the typical irradiation schemes most commonly used in laser pulse initiated time-resolved EPR and ENDOR methods to characterize transient intermediates of photoprocesses. They represent examples of the rapidly expanding area of modern EPR spectroscopy which presently provides spectacular new possibilities similar to what happened decades ago with the advent of pulsed NMR spectroscopy. The experimental challenge is to detect the spectral and temporal development of the laser-induced transient EPR response in the ns time range.

In standard EPR spectroscopy with continuous wave (cw) microwave irradiation and modulation (typically at 100 kHz) of the linearly swept magnetic field with narrow-band phase sensitive (lock-in) detection of the signal (see Fig. 5a), the time response is limited to the 100 μs range. In practice, this can be

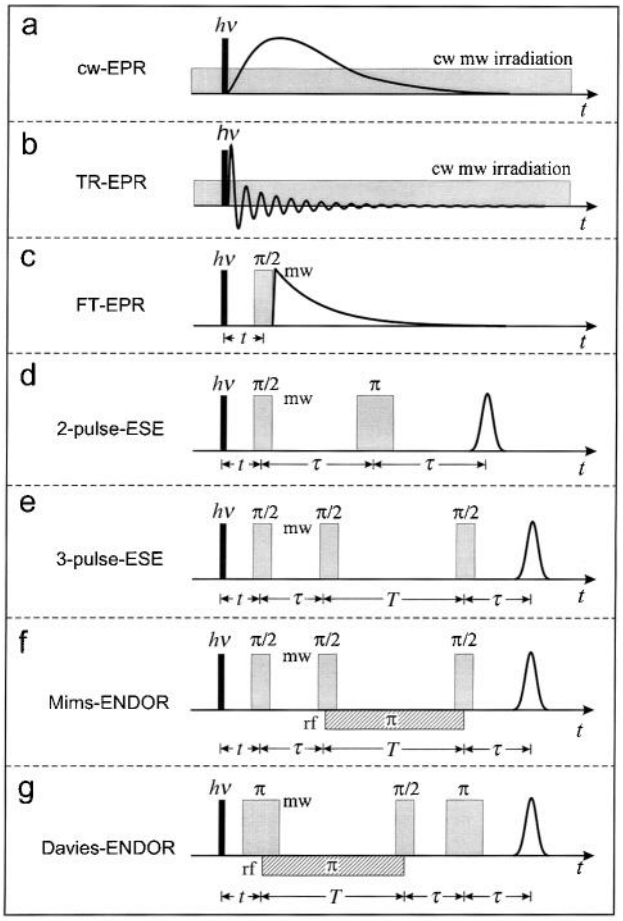

Fig. 5 Microwave (mw) and radio-frequency (rf) irradiation schemes of various time-resolved EPR techniques. The initial laser excitation pulse hν starts the photochemical radical generation. For details, see text.

shortened by another order of magnitude by going to higher modulation frequencies up to the MHz region. A decisive step forward in time resolution to the 10 ns range, however, is achieved by abandoning the modulation and lock-in detection techniques. Instead, one resorts to methods of direct detection of the transient nutation EPR signal (TR-EPR) employing fast data acquisition systems while stepping through the magnetic field. For a particular field value this signal is shown in Fig. 5b. For sufficiently broad inhomogeneous line widths, the initial signal rise time is no longer determined by the microwave field amplitude but is governed by the inverse of the EPR line width.[16] In the case of broad EPR lines around 50 MHz typical for biochemical samples, the time resolution is only limited by the instrumental response time that by now has been pushed to the 10 ns range.

Fortunately, in light-flash initiated photoprocesses, such as laser-induced photosynthetic electron transfer, the reduced sensitivity of the broad-band TR-EPR methods can be largely compensated by exploiting process-inherent electron spin-polarization effects (see section 5).

In analogy to modern NMR spectroscopy, pulsed microwave excitation of the electron spin system now offers a variety of EPR methods of high temporal and spectral resolution, in particular in the form of two-dimensional (2D) spectroscopy.[17] In Fig. 5c, the basis of Fourier-transform (FT)-EPR on laser-induced radicals is sketched: at varying delay times after the laser pulse the free-induction-decay (FID) signal is recorded after the magnetization of the whole spectrum (or parts of it in the case of broad spectra) has been tilted by 90° by a short, intense $\pi/2$ pulse. FT-EPR and transient nutation TR-EPR techniques are complementary to each other for investigating photoprocesses. In the case of narrow lines, as are typical for free radicals in solution, FT-EPR has a multiplex advantage in signal averaging efficiency; in the case of broad lines, as are typical for short-lived transients in frozen solution or soft glass media, TR-EPR can be applied without being restricted by limited microwave field amplitudes.[5]

Very versatile, in terms of narrow or broad spectra, are the pulsed spin-echo EPR methods that have now become feasible due to improved microwave and data acquisition technologies. The general principle of the two-pulse echo experiment (Hahn-echo, E. Hahn, 1950) is shown in Fig. 5d. In the external B_0 field that is applied along the *z*-axis, the light-generated net spin magnetization is parallel to *z*. A $\pi/2$ pulse along the *x*-axis turns the magnetization along the *y*-axis. The spin packets now precess around the *z*-axis in the *x*–*y* plane and, owing to inhomogeneities in the local fields seen by the spins, start to dephase during this precession. After a delay time τ, a second pulse of 180° duration reverses the electron spin precession thereby refocusing the spin packets, *i.e.*, leading to the formation of an electron spin echo (ESE) after time τ. The amplitude of the two-pulse spin echo, $S(2\tau, B_0)$, at a given field value B_0 of the spectrum, decays exponentially with the 'phase memory' time T_M. By stepping B_0 through the resonance region and varying the pulse separation time τ, an ESE-detected EPR spectrum can be recorded in two dimensions, whose slices at the different B_0 or τ values provide kinetic or spectral information, respectively.

When ESE spectroscopy is applied to samples with inhomogeneously broadened cw-EPR lines, a situation which is typical for biological systems due to unresolved hyperfine interactions, the measured T_M is equal to T_2, the spin–spin relaxation time which determines the homogeneous line width of a single spin packet.[18] This is of utmost importance for studies of molecular motions: while ESE experiments provide the homogeneous line width parameters directly, the lineshape analysis of cw-EPR spectra is often severely hampered by inhomogeneous broadening. Thus, it is very difficult to distinguish between inhomogeneous and motional contributions to line broadening in cw-EPR (see section 5).

An important variant of the Hahn-type two-pulse sequence is the three-pulse 'stimulated' echo sequence (see Fig. 5e). In this sequence the π pulse of the Hahn-echo experiment is split into two $\pi/2$ pulses separated by a waiting time *T*. After the first two $\pi/2$ pulses that are separated by τ, components of the dephased magnetization pattern are stored along the *z*-axis where they remain during the time *T*. This waiting time is varied, but chosen to remain shorter than T_1, the spin-lattice relaxation time, which governs the decay of the *z*-component of the magnetization. The third $\pi/2$ pulse turns these *z*-components back into the *xy*-plane where they give rise to a stimulated echo at time τ after the third pulse. The characteristic time constant for the stimulated echo decay as a function of *T* is much longer than the phase-memory time T_M. This is because the phase information has been stored along the *z*-axis where it can only decay by T_1 processes. In general, the stimulated echo decays with a time constant between T_1 and T_2, *i.e.*, in soft glass or frozen solution samples with $T_1 >> T_2$ the stimulated echo persists much longer than the Hahn-echo. The experimental requirement for observing spin echoes is that the pulse lengths have to be short compared to T_2. In contrast to NMR, this requirement can become a formidable task in EPR, in particular for broad lines, as are typical for biological systems.

To determine hyperfine interactions, in the first part of this section cw methods were described, cw-ENDOR and electron-nuclear-nuclear triple resonance being the most important examples. There are, however, also time-resolved ENDOR methods, which in certain situations are superior. They either employ cw microwave and radio-frequency fields and use direct detection, or they employ microwave and radio-frequency pulses and use ESE detection. The first variant is an ENDOR extension of the transient nutation TR-EPR method.[19] Recently, it was applied to photo-excited spin-polarized triplet states of

the primary donor P_{680} of PS II,[14] and also to triplet model systems, such as porphyrins and chlorins.[20] The pulsed methods for detecting hyperfine interactions are rapidly expanding, and specialized overviews exist already, for instance by Schweiger.[17] In short, one can say that both ENDOR methods, *i.e.*, with cw or pulsed irradiation schemes, have their merits and limitations depending on the specific sample under study. For optimum cw-ENDOR, in terms of signal intensity and resolution, a critical balance has to be created between saturation and relaxation of electron and nuclear spins.[12] This requires the proper choice of solvent, temperature and power of the irradiation fields. In the case of protein systems, this balance is often difficult to establish. For pulsed ENDOR, an electron spin echo has to be created of sufficiently long lifetime to allow manipulation of the nuclear spins by radio-frequency irradiation. If the microwave pulse sequences are chosen in such a way that the electron spin magnetization is essentially stored along the *z*-axis (see Figs. 5f, 5g), optimum pulsed ENDOR requires a sufficiently long spin-lattice relaxation time T_1. This can often be achieved by temperature selection, even for biological systems. Accordingly, with pulsed irradiation schemes the ENDOR response is generally larger than with cw irradiation (typically 50% of the EPR signal as compared to 10% for cw-ENDOR.

In the following we only mention those pulsed techniques for measuring hyperfine couplings that are frequently used in photosynthesis research. There is one technique that does not need radio-frequency irradiation at all, but measures nuclear modulations of the electron spin echo envelope as a function of the microwave pulse separation. The occurrence of 'ESE Envelope Modulations' (ESEEM) is restricted to solid-state samples, as it requires interactions of anisotropic dipolar hyperfine tensor components. Hence, after Fourier transformation of the modulated echo decay, an ENDOR frequency spectrum is obtained. In the three-pulse ESE, the ESEEM intensity modulations are sustained much longer than in the two-pulse ESE, because the echo decay is determined by T_1 rather than by the much shorter T_2. The correspondingly increased number of modulations leads to sharper ESEEM lines in the three-pulse spectra. For a sufficiently large depth of the modulations, the hyperfine and nuclear Zeeman interactions have to be comparable in magnitude to allow for effective mixing of the nuclear spin function by the dipolar interaction with the electron spin ('cancellation condition'). Consequently, for maximum modulation depth an optimum Zeeman field B_0 exists for each hyperfine coupling. At X-band, ESEEM spectroscopy, therefore, is best suited for weakly coupled nuclei. At higher B_0 fields larger hyperfine couplings also become accessible.[21]

On the other hand, large hyperfine interactions can favorably be measured by pulsed ENDOR spectroscopy. The two commonly used versions are Mims-type (W. B. Mims, 1972) and Davies-type (E. R. Davies, 1974) ENDOR. Figs. 5f and 5g show the pulse sequences of the microwave (mw) and radio-frequency (rf) channels of Mims- and Davies-ENDOR, respectively. The advantages and drawbacks of both types of pulsed ENDOR are discussed in the literature.[22]

4 High-field/high-frequency EPR and ENDOR

From the spin Hamiltonians (eqns. (3), (7)) one sees that some interactions are magnetic field-dependent (the Zeeman interactions), while others are not (the fine and hyperfine structure interactions). Obviously, in complex biological systems it will be necessary to measure at various field/frequency settings in order to separate these interactions from each other. Up to now, cw and time-resolved EPR studies on photosynthetic samples have been concentrated on standard X-band frequencies (9.5 GHz), extensions to lower (S-band, 4 GHz) and higher microwave frequencies (K-band, 24 GHz; Q-band, 35 GHz) are exceptions. 'True' high-field/high-frequency EPR is generally accepted to start at the W-band (95 GHz), (see below). Its recent application to photosynthesis has provided a realm of new insights concerning spatial and electronic structures of the charge-separated cofactors interacting with their protein environment, as well as concerning their molecular motion in the binding sites. In the following, an account of this high-field EPR work is presented.

For low-symmetry systems, particularly in frozen solution samples, standard EPR suffers from low spectral resolution. Such problems arise, for instance, because several radical species or different magnetic sites of rather similar *g*-values are present or a small *g*-factor anisotropy of the paramagnetic system does not allow canonical orientations of the powder EPR spectrum to be observed. In such a case, even ENDOR does not provide single-crystal-type information on the hyperfine structure. For defining a lower limit of the microwave frequency and corresponding magnetic field B_0 for true high-field EPR, we relate properties of the spectrometer with properties of the sample. For all cases of delocalized spin systems, in which unresolved hyperfine interactions dominate the inhomogeneous EPR line width, a true high-field experiment must fulfil the condition (11), *i.e.*, the anisotropic Zeeman interaction must

$$\frac{\Delta g}{g_{\mathrm{iso}}} \cdot B_0 > \Delta B_{1/2}^{\mathrm{hf}} \tag{11}$$

exceed the inhomogeneous line broadening. For example, for deuterated samples Q-band EPR might already fulfil this condition in the case of semiquinone radicals with rather large *g*-anisotropy, whereas for protonated samples with larger line widths, it does not. On the other hand, in the case of chlorophyll ion radicals, due to their small *g*-anisotropy, even W-band EPR might not meet the high-field condition for protonated samples, but deuteration is necessary or 360 GHz EPR (see below). At sufficiently high microwave frequencies ν_0 and applying correspondingly high magnetic fields B_0, the spectral resolution can be dramatically improved, because eqn. (12) holds, where

$$\Delta B_0 = \frac{h\nu_0}{\mu_{\mathrm{B}}}\left(\frac{1}{g_1} - \frac{1}{g_2}\right) \tag{12}$$

ΔB_0 is the difference in resonance field positions for *g*-values g_1, g_2. Except for transition metal complexes, most bioorganic systems have $g \approx 2$, and relative *g* variations $\Delta g/g$ rarely exceed 10^{-4}–10^{-3}. At X-band frequencies the corresponding ΔB_0 values are only 0.03–0.3 mT, which can easily be masked in disordered samples with typical EPR line widths around 1 mT. Fortunately, for many bioorganic systems the increase of ΔB_0 with increasing Zeeman field directly translates into an increase of spectral resolution, because often no noticeable line broadening occurs with increasing B_0 up to about 15 T. Double resonance extension to high-field ENDOR then has the additional advantage of providing single-crystal-like hyperfine information, in the reference frame of the $\tilde{g}$ tensor, even from disordered samples with very small *g*-anisotropy (see below).

Also for high-spin systems ($S > 1/2$), high-field EPR might be advantageous. Although the fine-structure term, eqn. (7), is not field-dependent it leads, in combination with the electronic Zeeman term, to a field-dependent mixing of the electron spin eigenfunctions. At zero field, the triplet spin eigenfunctions, T_x, T_y, T_z, are quantized along the molecular axes system (*x*, *y*, *z*). At high field, the magnetic spin quantum number, $m_S = +1, 0, -1$, is a good quantum number, and the spin eigenfunctions become T_{+1}, T_0, T_{-1}. If the external field values B_0 are such that the electron Zeeman and the fine-structure splittings are comparable in magnitude, the spin functions become mixed functions of both bases, the degree of mixing depending on B_0 and the relative orientation of the molecule with respect to the field. As a consequence, the triplet energy eigenvalues of the

different electron wave functions are not linearly related to the strength of B_0 (see Fig. 4a). This intermediate region requires more complicated calculations to analyze the EPR spectrum. One more reason to perform high-field EPR, therefore, is to simplify the spectrum analysis. Moreover, the hyperfine lines of high-spin systems usually get narrower at higher magnetic fields than in X-band EPR because of second order effects: if we take Mn^{2+} centers (S = 5/2, I = 5/2) in disordered protein samples as an example, the EPR transitions are strongly broadened by contributions from the zero-field tensor. Hence, normally only the $m_S = -1/2 \leftrightarrow +1/2$ transition is observable, due to its smallest orientation dependence. Also this transition is split into six hyperfine lines; their line width, $\Delta B_{1/2}$, is determined by second-order contributions from the zero-field coupling D [eqn. (13)]. Applying high-field/high-frequency

$$\Delta B_{1/2} \propto D^2/B_0 \qquad (13)$$

EPR leads to a reduction of these line width contributions and, indeed, 'needle sharp' manganese hyperfine lines are observed in 95 GHz EPR spectra of Mn^{2+} protein complexes such as PS II, even in disordered samples.

This behavior is exploited by many high-field EPR spectroscopists who use Mn^{2+} ions doped into MgO powder as a reference sample for precise g-factor and field calibration measurements.[23] Up to second order, the EPR resonance fields of the six Mn^{2+} hyperfine components, $m_I = -5/2, \ldots +5/2$, are given by eqn. (14), where a is the isotropic hyperfine coupling;

$$B_{m_I} = B_0 - a \cdot m_I - (a^2/2\,B_0)\,[I(I+1) - m_I^2 \qquad (14)$$

the g-factor is contained in the Zeeman field $B_0 = F\nu_0/g$ (ν_0 microwave frequency, $F = h/\mu_B = 71.447751$ mT GHz^{-1}). The high precision reference data are: $g(Mn^{2+}) = 2.00101 \pm 0.00005$ and $a(Mn^{2+}) = -(8.710 \pm 0.0003)$ mT.[23]

With these advantages in mind, over the last 15 years a small number of laboratories accepted the technological challenge to construct millimeter and submillimeter high-field EPR spectrometers, thereby tilling the ground of a promising new research area. The pioneering work in this endeavor was done by Y. S. Lebedev and his collaborators (see citation 104 in ref. 5) in Moscow (1976). Recently high-field EPR spectrometers have also become commercially available. The physical principles and technical aspects have been published by the laboratories involved, and appropriate references are included in recent overview articles, for instance in ref.[5]

Details of the laboratory-built Berlin W-band EPR/ENDOR spectrometer are given in ref. 23 for the cw and in ref. 24 for the pulsed mode of operation, including details of the 95 GHz probeheads, a Fabry-Perot resonator and a cylindrical TE_{011} cavity. For small single-crystal samples, the EPR sensitivity is about 4×10^8 spins mT^{-1}, *i.e.*, about three orders of magnitude higher than at standard X-band frequencies. The time-resolution of the heterodyne detection channel is about 5 ns, and a 90° pulse of 40 ns is achieved with a mw power of 10 mW at the cylindrical cavity. In contrast to pulsed X-band spectrometers, the detection channel of the W-band spectrometer is practically dead-time free. Very recently, the Berlin group has completed the construction of the first 360 GHz, 14 T EPR spectrometer which allows resolution of the extremely small g-anisotropies of chlorophyll cofactor radicals.[25]

5 High-field/high-frequency EPR/ENDOR applications in photosynthesis

In the following section selected examples of recent applications of high-field EPR and ENDOR spectroscopy are reported, emphasizing radicals and radical pairs involved as intermediates in primary processes of *bacterial* photosynthesis. *Plant* photosynthesis will be dealt with only briefly at the end of this section.

5.1 Bacterial photosynthesis

For RCs of several photosynthetic purple bacteria high-resolution X-ray structures exist, for instance of *Rb. sphaeroides* (see section 2). The availability of such three-dimensional structures has paved the way for the on-going systematic elucidation of the structure–function relationship of bacterial photosynthesis on the molecular level. For *Rb. sphaeroides* single-crystal RCs, for example, from recent X-band EPR, ENDOR and electron-nuclear-nuclear triple resonance studies of $P_{865}^{+\cdot}$, the electronic structure of the bacteriochlorophyll dimer could be elucidated in great detail on the basis of the X-ray structure[13] (see above). These ENDOR experiments demonstrate that even for large bioorganic systems subtle details of the electronic structure and distortions by environmental effects can be explored by probing the *local* properties of the unpaired electron wavefunctions *via* hyperfine interactions. On the other hand, the unambiguous assignment of hyperfine couplings to molecular positions generally poses great problems and can often be solved only by elaborate isotope labeling and/or single-crystal experiments. It is, therefore, desirable to also use the electronic $\tilde{g}$ tensor, reflecting the *global* properties of the wavefunction, for probing the electronic structure of the cofactor radicals in interaction with their protein environment. Since the g-anisotropy of many bioradicals is less than 10^{-3}, high-field EPR is mandatory for measuring the $\tilde{g}$ tensor components with sufficient accuracy. In the following we summarize 95 GHz (W-band) EPR and ENDOR results obtained in the Berlin high-field EPR laboratory from transient radicals and radical pairs in RCs of *Rb. sphaeroides*.

5.1.1 Primary donor. One of the intriguing puzzles in bacterial photosynthesis is the so-called unidirectionality of the photoinduced ET, *i.e.*, the electron is transferred preferentially along the L protein subunit, despite the approximate C_2 symmetry of the cofactor location in the L and M proteins (see section 2). In an attempt to determine, by means of the global $\tilde{g}$ tensor probe, the characteristic symmetry properties of the electronic structure of the primary donor, 95 GHz high-field EPR on illuminated single-crystal RCs of *Rb. sphaeroides* was performed at 12 °C.[26] At a field of 3.3 T even the magnetically inequivalent sites in the unit cell of the RC crystal could be resolved, and the angular dependence of their g-factors in the three symmetry planes of the crystal has been measured and analyzed. The data analysis was accomplished by applying eqn. (5).

As is seen from Fig. 6, the principal directions (α, β, γ) of the $\tilde{g}$ tensor in the molecular axes system (x, y, z) reveal a breaking of the local C_2 symmetry in the electronic structure of $P_{865}^{+\cdot}$. This finding is consistent with earlier ENDOR results for the hyperfine structure (see above). High-field EPR (95 GHz) on RC single crystals was also used to characterize the $\tilde{g}$ tensor of $P_{865}^{+\cdot}$ in the heterodimer mutant HL(M202) of *Rb. sphaeroides*.[27] Since in this mutant the unpaired electron of $P_{865}^{+\cdot}$ is localized on the bacteriochlorophyll, the $\tilde{g}$ tensor reflects the monomer properties. The directions of the principal axes of the $\tilde{g}$ tensor are similar for the mutant and the wild type.

With the availability of precise $\tilde{g}$ tensor data, there is an increasing need for a reliable quantum-mechanical analysis of $\tilde{g}$ tensors of biomolecules. This is a demanding endeavor,[28] and state-of-the-art publications in this field have been reviewed recently.[5]

It remains to be seen whether the breaking of C_2 symmetry in $P^{+\cdot}$ is a relevant factor in controlling the unidirectional ET in primary bacterial photosynthesis. Other factors could contribute, such as cofactor- or protein-mediated superexchange to modify the electronic coupling in the long-distance ET along the L protein subunit and/or dielectric asymmetry of the RC protein complex along the two potential ET pathways. Many more organisms, both wild types and mutants, will have to be

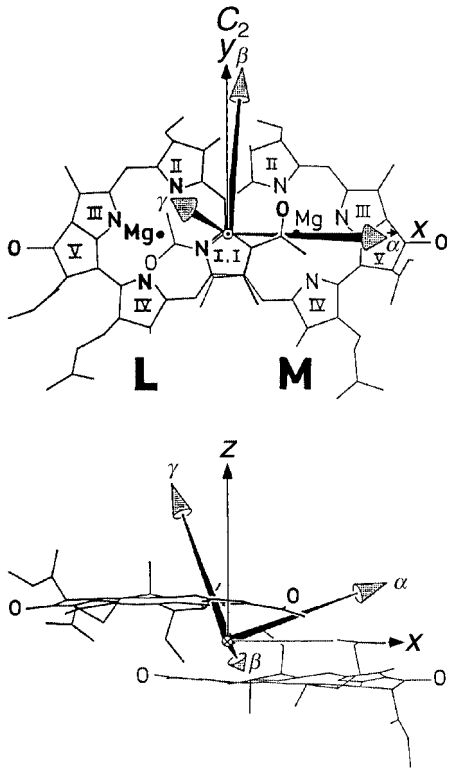

Fig. 6 Principal $\tilde{g}$ tensor axes system (α, β, γ) and molecular axes system (x, y, z) of $P_{865}^{+\cdot}$ in single-crystal RCs of *Rb. sphaeroides* as determined by W-band high-field EPR.[26] (Top) View from the z-direction onto the BChl dimer planes. (Bottom) Side view into the direction of the local C_2 symmetry axis (y-axis). Notice that the $\tilde{g}$ tensor orientation deviates from the molecular C_2 symmetry.

studied in detail before a definite conclusion can be reached regarding these other factors. The results for the doublet state, $P^{+\cdot}$, should also be compared with those for the photoexcited triplet state, ^{T}P, since the *orientation* of the zero-field-splitting tensor is a sensitive probe for the symmetry properties of the triplet-state wave function extending over the dimer halves.[2]

5.1.2 Quinone acceptors. Quinones play an important role in many biological systems, prominent examples being the light-driven ET processes of photosynthesis. In the photosynthetic bacterium *Rb. sphaeroides*, for example, the primary and secondary quinones, Q_A and Q_B, act as one- and two-electron gates, respectively: $Q_A^{-\cdot}$ just passes the extra electron to Q_B which, in a second photo-initiated ET step, gets doubly reduced, binds two protons, dissociates from the RC, and releases the protons on the periplasmic side of the membrane. In *Rb. sphaeroides*, Q_A and Q_B are the same ubiquinones-10; obviously their different functions in the ET processes are induced by different interactions with their protein environment.

High-field EPR and ENDOR experiments on quinone radical anions in frozen RC and propan-2-ol solutions were performed at W-band frequencies to measure anisotropic $\tilde{g}$ and hyperfine tensor components, respectively. The aim was to learn about the anisotropic interactions with the protein environment, such as hydrogen bonding to specific amino acid residues, and about the motional dynamics of the quinones in their binding sites. From more than a dozen quinone anion radicals, both natural and model systems, powder high-field EPR spectra were recorded. Owing to the high Zeeman magnetoselection capability of W-band EPR, a high degree of orientational selectivity is achieved that is unaccessible by X-band EPR (compare Figs. 7a and 7b).[29,30] The measured $\tilde{g}$ tensor components follow the sequence $g_{xx} > g_{yy} > g_{zz}$, where x is along the –C = O bond direction, and z is perpendicular to the quinone plane.

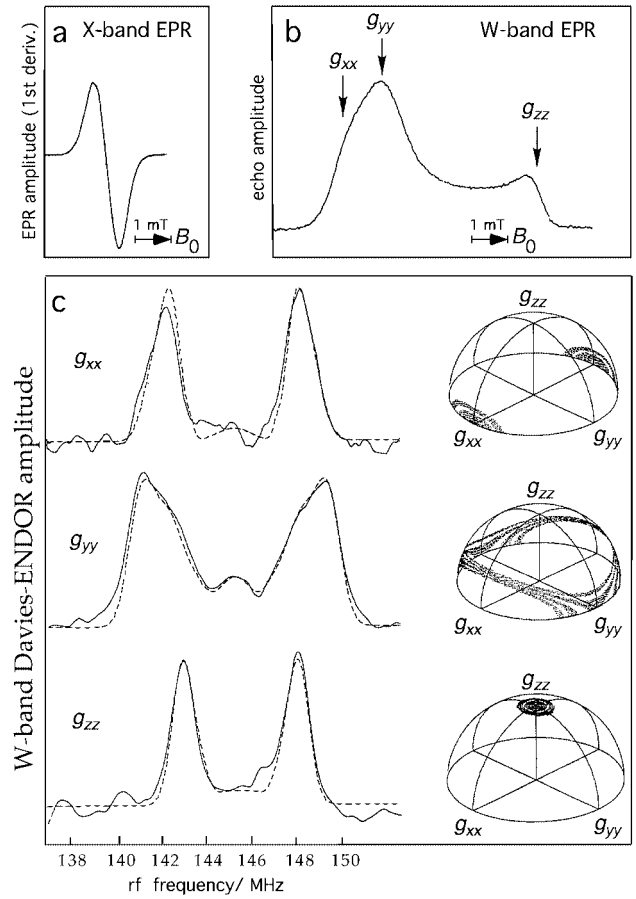

Fig. 7(a) X-band cw-detected and (b) W-band ESE-detected EPR spectra of ubiquinone-10 anion radicals in frozen perdeuterated propan-2-ol solution (T = 115 K). (c) Davies-ENDOR spectra taken at the three B_0 positions marked in (b) that represent the canonical $\tilde{g}$ tensor orientations. Dotted lines show the simulated ENDOR spectra from which the degrees of orientation selection of contributing molecules (right) was derived.[30]

Exploiting the Zeeman magnetoselection even further, W-band pulsed ENDOR was performed at the rather well separated canonical peaks of the powder EPR spectrum. Fig. 7c shows the Davies-type ENDOR spectra of the radical anion of ubiquinone-10 in frozen perdeuterated propan-2-ol at T = 115 K. (For the Davies-ENDOR pulse sequence, see Fig. 5g). At least for the g_{xx} and g_{zz} canonical field positions, the ENDOR spectra are single-crystal-like and, accordingly, the representations of the orientational selections of molecules show narrow distributions (see right side of Fig. 7c). These representations follow from the simulations of the spectra on the basis of the spin Hamiltonian of eqn. (3). The orientational distribution of molecules is considerably broader for the g_{yy} canonical value, which reflects its still rather poor resolution by W-band EPR. When varying the solvent (protic and aprotic, with and without perdeuteration), characteristic changes of hyperfine couplings (predominantly along the y-direction) and $\tilde{g}$ tensor components (predominantly along the x-direction) could be discerned. They are attributed to hydrogen-bond formation at the lone-pair orbitals on the oxygens. Dipolar hyperfine interactions with the solvent protons will result in line broadening along the oxygen lone-pair direction, *i.e.*, broadening of the g_{yy} part of the EPR spectrum, while changes in the lone-pair excitation energy $\Delta E_{n\pi^*}$ and/or spin density ρ_O^{π} at the oxygen due to H-bonding will predominantly shift the g_{xx} component of the $\tilde{g}$ tensor.[29]

Besides *static* cofactor–protein interactions as a controlling factor for enzyme activity, *dynamic* properties of cofactors in their binding sites are also of particular relevance. This also holds for the primary processes in photosynthesis if the time constant of a characteristic molecular motion becomes comparable to one of the time constants, k_{ET}^{-1}, in the ET chain for charge separation (see Fig. 2) or recombination (which are

orders of magnitude slower). For this reason, there is an increasing interest in the slow motional modes of thermal fluctuations of protein–cofactor complexes. They may affect the electron tunnelling mechanism and thereby the biological function. In order to learn more about slow motions of the quinone cofactors in photosynthesis, the anisotropic stochastic oscillatory motions of $Q_A^{-\cdot}$ in frozen RC solutions of *Rb. sphaeroides* have been studied by pulsed 95 GHz high-field EPR methods.[31] The two-dimensional field-swept electron spin echo (ESE) technique (see Fig. 5d) was chosen for this experiment because it directly reveals the homogeneous line width parameter T_2 and, due to the high field, resolves its

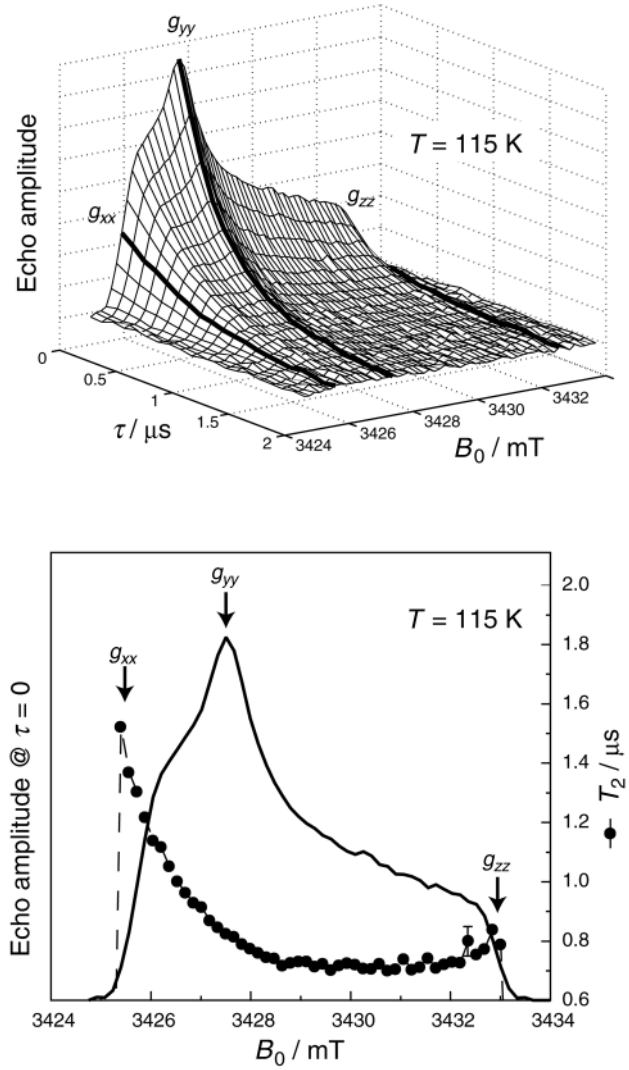

Fig. 8 (Top) Field-swept two-pulse echo decay spectrum of $Q_A^{-\cdot}$ in frozen-solution RCs (T = 115 K) of the $Fe^{2+} \rightarrow Zn^{2+}$ mutant HC(M266) of *Rb. sphaeroides*.[32] (Bottom) Extrapolated τ = 0 slice of the ESE-detected EPR spectrum and field-dependent T_2 relaxation times, as extracted from the decay functions $S(2\tau, B_0) = S_0 \cdot \exp(-2\tau/T_2(B_0))$. For details, see ref. 31.

variation over the powder spectrum. Fig. 8 (top)[32] shows the two-dimensional W-band ESE spectrum of $Q_A^{-\cdot}$ in frozen-solution RCs of the *Rb. sphaeroides* mutant HC(M266), in which Fe^{2+} is replaced by Zn^{2+}, at 115 K. The canonical orientations of the $\tilde{g}$ tensor are rather well resolved at this field. The monoexponential echo decay curves at the g_{xx}, g_{yy} and g_{zz} orientations are emphasized in Fig. 8. Obviously, the decays have different time constants T_2 in different directions. Since T_2 relates solely to the dynamic process, the resolved anisotropy of T_2 directly provides information about the axes of torsional fluctuations of $Q_A^{-\cdot}$ at a given temperature. As is shown in Fig. 8 (bottom),[32] at T = 115 K the magnitude of T_2 varies over the powder EPR spectrum and clearly peaks at the g_{xx} orientation.

At high B_0 fields, the dominant contribution to anisotropic T_2 relaxation stems from the wobbling motion of $Q_A^{-\cdot}$, and depends on the orientation of the $\tilde{g}$ tensor with respect to the $\mathbf{B_0}$ direction

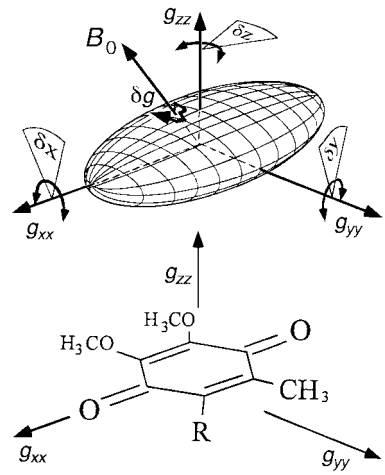

Fig. 9 Schematic representation of the $\tilde{g}$ tensor connected with $Q_A^{-\cdot}$ (R stands for the isoprenoid chain). When $Q_A^{-\cdot}$ undergoes stochastic thermal fluctuations with angular amplitudes δx, δy, δz, the $\tilde{g}$ tensor orientation fluctuates with respect to $\mathbf{B_0}$. This causes g-factor fluctuations δg of varying magnitude and thereby anisotropic T_2 relaxation. For details, see ref. 31.

(see Fig. 9). The magnitudes of the T_2 contributions are determined by random walk on the surface of the $\tilde{g}$ tensor ellipsoid. This leads to time- and angular-dependent fluctuations δg that translate to fluctuations of the Larmor frequency of the electron spins. As is obvious from Fig. 9, the Larmor frequency fluctuations will be minimal for $Q_A^{-\cdot}$ oscillations around the principal axes x, y, z. In other words: the T_2 values will be the largest along the directions of the respective axes of oscillation. Thus, the maximum of T_2 in the g_{xx} region (see Fig. 8 bottom) tells us that, at 115 K, the wobbling motion of $Q_A^{-\cdot}$ predominantly occurs around the x-direction, *i.e.*, along the –C=O bond direction. By inspection of the X-ray structure of the Q_A binding site, one can conclude that this finding reflects the hydrogen bond situation of the Q_A site: the most probable H-bond partners of Q_A are histidine (M219) and alanine (M260). They provide the x-axis of torsional fluctuations of Q_A at low temperature. Obviously, the next steps in this molecular dynamics study will be to go to higher temperatures and look for effects of protein conformational changes, and to go to the secondary quinone, Q_B, with its pronounced differences in amino acid environment as compared to the Q_A site. Work along these lines is in progress in the Berlin laboratory.

5.1.3 Correlated radical pairs. Pulsed W-band EPR experiments on the short-lived $P_{865}^{+\cdot}$ $Q_A^{-\cdot}$ radical pair in frozen RC solution of *Rb. sphaeroides* allowed the determination of the three-dimensional structure of the charge-separated donor–acceptor system.[33] On physical grounds, this might differ from the ground-state structure and, indeed, upon illumination drastic changes have been observed recently in the X-ray structure of the Q_B binding site of *Rb. sphaeroides*.[34] The high-field EPR spectra were recorded using the field-swept two-pulse echo technique (see Fig. 5d). To avoid fast spin relaxation of the $Q_A^{-\cdot}$, the non-heme Fe^{2+} ion was replaced by Zn^{2+}. The charge-separated radical pairs $P_{865}^{+\cdot}$ $Q_A^{-\cdot}$ were generated by 10-ns laser flashes. Their time-resolved EPR spectrum is strongly electron spin-polarized because the transient radical pair is suddenly born in a spin-correlated non-eigenstate of the spin Hamiltonian with pure singlet character.[33] Such spin-polarized spectra with lines in enhanced absorption and emission (see Fig. 10) contain important structural information of magnitude and orientation

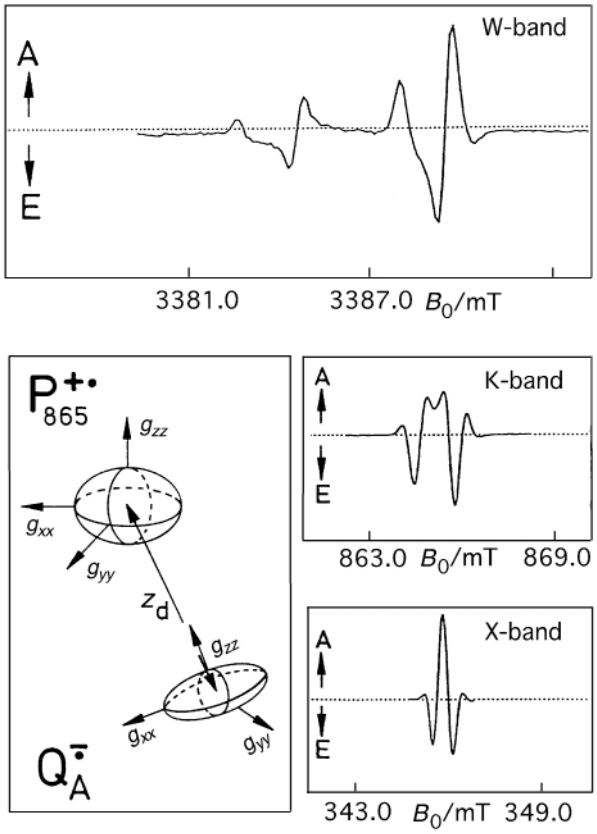

Fig. 10 Schematic representation of relative orientations of the $\tilde{g}$ tensors and dipolar axis z_d of the transient radical pair $P^{+\cdot}_{865}Q^{-\cdot}_A$ of *Rb. sphaeroides*. Its spin-polarized EPR spectra of frozen RC solutions are recorded at various settings of microwave frequency and magnetic field. A, E stand for absorption, emission. For details, see ref. 33.

of the $\tilde{g}$ tensors of the two radical partners, $P^{+\cdot}_{865}$ and $Q^{-\cdot}_A$, with respect to each other and to the dipolar axis z_d connecting the two radicals (see Fig. 10). Several parameters critically determine the lineshape of the polarization pattern,[33] such as the principal values of the $\tilde{g}$ and dipolar coupling tensors, the exchange coupling *J*, and the inhomogeneous line width of both radicals. These parameters were determined independently in order to obtain meaningful simulations of the spin-polarized spectra. From earlier time-resolved EPR measurements[5] on the radical pair $P^{+\cdot}_{865}$ $Q^{-\cdot}_A$, at X-band (9.5 GHz), K-band (24 GHz) and Q-band (35 GHz), $\tilde{g}$ tensor orientations could not be extracted unambiguously from simulations of the spin-polarized spectra. This was mainly because of strongly overlapping lines, even when deuterated samples were used to reduce hyperfine contributions. In the pulsed W-band experiments, however, the Zeeman field is strong enough to largely separate the inhomogeneously broadened contributions from $P^{+\cdot}_{865}$ and $Q^{-\cdot}_A$. Thus, the overall spectrum is dominated by the anisotropies and differences of the two $\tilde{g}$ tensors. Thereby the interpretation of the polarized spectrum is simplified and allows an unambiguous analysis of the tensor orientations. The most important result of this high-field EPR study is that, within an error margin of ±0.3Å, no light-induced structural changes of the $Q^{-\cdot}_A$ site with respect to $P^{+\cdot}_{865}$ occur, as compared to the ground-state configuration $P_{865}Q_A$. This finding is in accordance with recent results from various other studies, including X-ray crystallography.[34]

Generally, we believe that by pulsed high-field EPR experiments on spin-correlated coupled radical pairs ET-induced structural changes in the relative orientation of donor and acceptor can be detected with high precision, even for disordered samples. Such information is very desirable for a detailed understanding of the ET characteristics on the molecular level. One should keep in mind that the charge-separated radical pair state represents the working state for ET recombination.

5.2 Plant photosynthesis

Our understanding of the structure–function relationship for the primary processes in plant photosynthesis is still in its infancy mainly because the three-dimensional structures of PS I and PS II are not yet known with sufficient accuracy. This situation is in contrast to that of RCs of purple photosynthetic bacteria (see section 2).

Taking PS I as an example, the currently emerging X-ray structures, most recently at 4 Å resolution,[6] are still unable to even locate the quinone acceptor A_1, a phylloquinone. It was, therefore, a challenge to apply the whole arsenal of modern multifrequency time-resolved EPR and ENDOR techniques to PS I with the goal of determining the A_1 location and orientation (for a recent overview, see ref. 5). Also 95 GHz high-field two-dimensional ESE spectroscopy got involved in this game: it was applied to the spin-polarized radical pair $P^{+\cdot}_{700}A^{-\cdot}_1$ of the primary donor, P_{700}, and the A_1 quinone acceptor.[35] This experiment is similar to that on bacterial radical pairs, as described in section 5.1.3. A comparison of the spin-polarized spectra shows that the quinone acceptors are oriented differently with respect to $P^{+\cdot}$ in the RCs of *Rb. sphaeroides* and PS I. On the other hand, $P^{+\cdot}_{700}$ and $P^{+\cdot}_{865}$ have a similar structural arrangement with respect to the dipolar axis z_d connecting the radical pair partners.

Combining all pieces of information from the various EPR and ENDOR experiments, finally the goal of localizing A_1 in PS I was reached. Hence, multifrequency time-resolved EPR has again proven to be particularly suited for the characterization of the radical pair states in the RCs of different photosynthetic organisms.

Taking PS II as an example, one notices a growing interest in EPR studies of the tyrosyl radicals in the D1 and D2 polypeptides. In particular, the determination of individual $\tilde{g}$ tensor components in frozen PS II preparations by high-field/high-frequency EPR proved to be very informative in probing the different hydrogen bonding interactions of the Y_Z and Y_D tyrosyl and the Q_A and Q_B quinone radicals (see Fig. 1 and consult publications cited in ref. 4). Their frozen-solution spectra exhibit resolved Zeeman and, in some cases, hyperfine structure. Thus, they permit a detailed characterization of the radical centers in interaction with their micro-environment.

6 Conclusion

We have indicated in this overview how modern multifrequency EPR methods, in particular high-field EPR, provide detailed information about the structure and dynamics of the transient radicals and radical pairs that occur in photosynthetic electron transfer processes. Thereby our understanding of the relation between structure, dynamics and function is considerably improved. This is especially true with respect to the fine-tuning of electronic properties of donors and acceptors by means of weak interactions with their protein environment, such as hydrogen bonding to specific amino acid residues.

When we now look back at the title of this overview and ask for an answer to the question ‘what do we learn from high-field EPR?’, this answer can be given in terms of some summarizing statements: (1) Most organic cofactors in photosynthetic RCs have only small *g*-anisotropies and, therefore, require much higher fields than in X-band EPR to resolve the canonical $\tilde{g}$ tensor orientations in their powder spectra and, thereby, to trace orientation-selective hydrogen bonding in the binding sites. This is important complementary information to what is

available from X-ray diffraction. (2) In the course of the ET processes several radical species are often generated. To distinguish them by the small differences in their *g*-factor and hyperfine interactions, high fields are required. (3) This argument also holds for separating different sites of different cofactor orientations in the RC unit cell. (4) Often high-purity protein samples can be prepared only in minute quantities. This is the rule for protein crystals and RCs of site-directed mutants. Accordingly, to study them by EPR, very high sensitivity is needed. This can be accomplished only with dedicated high-field/high-frequency spectrometers. (5) High-field/high-frequency cw-EPR generally provides, by lineshape analysis, shorter time windows down into the ps range for studying correlation times of important dynamic processes, such as protein motion and folding over wide temperature ranges. (6) On the other hand, pulsed high-field/high-frequency EPR in the form of two-dimensional field-swept ESE spectroscopy gives real-time access to specific cofactor–protein slow motions on the ns time-scale, and even to their spatial anisotropy that is generated by anisotropic weak interactions within the binding site. (7) ENDOR at high Zeeman fields takes additional advantage of the magnetoselection of molecular subensembles in powder or frozen-solution samples. Thereby, even in the case of small *g*-anisotropies, ENDOR can provide single-crystal-like information about hyperfine interactions, including anisotropic hydrogen bonding to the protein. (8) By properly adjusting the Zeeman field in multifrequency pulsed EPR experiments, weakly and strongly interacting nuclei in the cofactor–protein system can be differentiated by their ESEEM and ENDOR spectra. (9) In metalloprotein high-spin systems, such as the Mn^{2+} oxygen-evolving complex in PS II, the EPR spectrum analysis can be drastically simplified at high fields due to suppression of second-order effects. Some high-spin metalloproteins with large zero-field splittings cannot be observed at all at X-band frequencies.

In concluding it is fair to state that time-resolved multifrequency EPR—in particular at high fields—has matured over recent years to present protein X-ray crystallographers and protein NMR spectroscopists with a powerful new ally for determining structure and dynamics of large organic biosystems. This new ally adds to the capability of determining structure–dynamics–function relations of such biosystems since transient intermediates can be observed in real-time while they are staying in their *working states* on biologically relevant time-scales. The role of high-field EPR in biology, chemistry and physics is rapidly growing. This growth has been recognized in recent years by an increasing number of national and international high-field EPR research programs and specialized symposia. Accordingly, the scientific literature on high-field EPR is also rapidly growing, and only a small sector could be covered in this overview.

7 Acknowledgements

Over the last years, numerous coworkers—students, postdocs, colleagues—from different parts of the world have contributed to the work presented. To all of them I want to express my gratitude. Their individual share in the work is highly appreciated and becomes evident by the references cited. Financial support of our work by the Deutsche Forschungsgemeinschaft is gratefully acknowledged.

8 References

1 J. Deisenhofer and J. R. Norris, *The Photosynthetic Reaction Center*, Academic Press, San Diego, 1993.
2 A. J. Hoff and J. Deisenhofer, *Phys. Rep.*, 1997, **287**, 1, and references therein.
3 M. Bixon, J. Fajer, G. Feher, J. H. Freed, D. Gamliel, A. J. Hoff, H. Levanon, K. Möbius, R. Nechushtai, J. R. Norris, A. Scherz, J. L. Sessler and D. Stehlik, *Isr. J. Chem.*, 1992, **32**, 369.
4 H. Levanon and K. Möbius, *Annu. Rev. Biophys. Biomol. Structure*, 1997, **26**, 495, and references therein.
5 D. Stehlik and K. Möbius, *Annu. Rev. Phys. Chem.*, 1997, **48**, 745, and references therein.
6 O. Klukas, W.-D. Schubert, P. Jordan, N. Krauss, P. Fromme, H. T. Witt and W. Saenger, *J. Biol. Chem.*, 1999, **274**, 7361.
7 K. H. Rhee, E. P. Morris, J. Barber and W. Kühlbrandt, *Nature*, 1998, **396**, 283.
8 C. R. D. Lancaster and H. Michel, *Photosynth. Res.*, 1996, **48**, 65, and references therein.
9 M. Bixon and J. Jortner, *J. Chem. Phys.*, 1997, **107**, 5154.
10 S. S. Skourtis, J. N. Onuchic and D. N. Beratan, *Inorg. Chim. Acta*, 1996, **243**, 167.
11 I. Daizadeh, E. S. Medvedev and A. A. Stuchebrukhov, *Proc. Natl. Acad. Sci. USA*, 1997, **94**, 3703.
12 K. Möbius, M. Plato and W. Lubitz, *Phys. Rep.*, 1982, **87**, 171, and references therein.
13 F. Lendzian, M. Huber, R. A. Isaacson, B. Endeward, M. Plato, B. Bönigk, K. Möbius, W. Lubitz and G. Feher, *Biochim. Biophys. Acta*, 1993, **1183**, 139.
14 M. Di Valentin, C. W. M. Kay, G. Giacometti and K. Möbius, *Chem. Phys. Lett.*, 1996, **248**, 434.
15 E. J. Reijerse, P. J. van Dam, A. A. K. Klaassen, W. R. Hagen, P. J. M. van Bentum and G. M. Smith, *Appl. Magn. Reson.*, 1998, **14**, 153.
16 D. Stehlik, C. Bock and M. C. Thurnauer, in *Advanced EPR, Applications in Biology and Biochemistry*, ed. A. J. Hoff, Elsevier, Amsterdam, 1989, ch. 11.
17 A. Schweiger, *J. Chem. Soc., Faraday Trans.*, 1995, **91**, 177.
18 J. Gorcester, G. L. Millhauser and J. H. Freed, in *Advanced EPR, Applications in Biology and Biochemistry*, ed. A. J. Hoff, Elsevier, Amsterdam, 1989, ch. 5.
19 F. Lendzian, P. Jaegermann and K. Möbius, *Chem. Phys. Lett.*, 1985, **120**, 195.
20 C. W. M. Kay, M. Di Valentin and K. Möbius, *J. Chem. Soc., Perkin Trans. 2*, 1997, 2563.
21 A. Bloeß, K. Möbius and T. F. Prisner, *J. Magn. Reson.*, 1998, **134**, 30.
22 A. Schweiger, *Pure Appl. Chem.*, 1992, **64**, 809.
23 O. Burghaus, M. Rohrer, T. Götzinger, M. Plato and K. Möbius, *Meas. Sci. Technol.*, 1992, **3**, 765.
24 T. F. Prisner, M. Rohrer and K. Möbius, *Appl. Magn. Reson.*, 1994, **7**, 167.
25 M. R. Fuchs, T. F. Prisner and K. Möbius, *Rev. Sci. Instrum.*, 1999, **70**, 3681.
26 R. Klette, J. T. Törring, M. Plato, K. Möbius, B. Bönigk and W. Lubitz, *J. Phys. Chem.*, 1993, **97**, 2015.
27 M. Huber and J. T. Törring, *Chem. Phys.*, 1995, **194**, 379.
28 J. T. Törring, S. Un, M. Knüpling, M. Plato and K. Möbius, *J. Chem. Phys.*, 1997, **107**, 3905.
29 M. Rohrer, M. Plato, F. MacMillan, Y. Grishin, W. Lubitz and K. Möbius, *J. Magn. Reson.*, 1995, **A116**, 59.
30 M. Rohrer, F. MacMillan, T. F. Prisner, A. T. Gardiner, K. Möbius and W. Lubitz, *J. Phys. Chem.*, 1998, **B102**, 4648.
31 M. Rohrer, P. Gast, K. Möbius and T. F. Prisner, *Chem. Phys. Lett.*, 1996, **259**, 523.
32 S. Weber, M. Fuhs, W. Hofbauer, W. Lubitz and K. Möbius, unpublished results, 1998.
33 T. F. Prisner, A. van der Est, R. Bittl, W. Lubitz, D. Stehlik and K. Möbius, *Chem. Phys.*, 1995, **194**, 361.
34 M. H. B. Stowell, T. M. McPhillips, D. C. Rees, S. M. Soltis, E. Abresch and G. Feher, *Science*, 1997, **276**, 812.
35 A. van der Est, T. F. Prisner, R. Bittl, P. Fromme, W. Lubitz, K. Möbius and D. Stehlik, *J. Phys. Chem.*, 1997, **B101**, 1437.

Review a706426h